INTERNATIONAL JOURNAL FOR NUMERICAL METHODS IN FLUIDS
Int. J. Numer. Meth. Fluids 2008; **57**:1269–1290
Published online 14 April 2008 in Wiley InterScience (www.interscience.wiley.com). DOI: 10.1002/fld.1790

Stabilized finite element methods to predict ventilation efficiency and thermal comfort in buildings

G. Lube[1,*,†], T. Knopp[2], G. Rapin[1], R. Gritzki[3] and M. Rösler [3]

[1]*Mathematics Department, Georg-August University Göttingen, D-37083 Göttingen, Germany*
[2]*Institute of Aerodynamics and Flow Technology, DLR Göttingen, D-37073 Göttingen, Germany*
[3]*Institute of Thermodynamics and Building Energy Systems, TU Dresden, D-01062 Dresden, Germany*

SUMMARY

The non-isothermal, incompressible Navier–Stokes equations with Boussinesq approximation are considered as a model of turbulent indoor air flows. The transient calculation is based on the Reynolds-averaged Navier–Stokes problem using the k/ε-turbulence model or improved variants such as the $\overline{v^2}-f$ model. The model is first discretized in time using backward-differencing schemes and then linearized using a Newton-type method per time step with emphasis on the proper calculation of (non-negative) turbulence quantities. The resulting auxiliary problems of Oseen type and of advection–diffusion–reaction type are solved using stabilized finite element method of residual type. Here we summarize some of our recent analytical results for higher-order methods and shock-capturing techniques. The numerical solution to the model in boundary layer regions is obtained using either adaptive wall functions if the k-ε model is used or a hybrid mesh with anisotropic refinement if the $\overline{v^2}-f$ model is applied. Besides the standard flow quantities, it is possible to calculate quantities such as the age of the air. Such quantities are used to develop criteria for the evaluation of the efficiency of air exchange in a room. The quality of the numerical simulations is demonstrated for typical benchmark problems. Copyright © 2008 John Wiley & Sons, Ltd.

Received 21 September 2007; Revised 17 January 2008; Accepted 4 February 2008

KEY WORDS: non-isothermal RANS model; stabilized FEM; indoor air flow; thermal comfort

1. INTRODUCTION

Turbulent flows driven or significantly affected by buoyancy occur in a variety of problems including building ventilation, cooling of electrical equipment, and environmental science. In this paper, turbulent indoor air flows are modelled by the non-isothermal, incompressible Navier–Stokes equations with Boussinesq approximation. In practice, such numerical simulations are nowadays still dominated by turbulence models based on the unsteady Reynolds-averaged Navier–Stokes

*Correspondence to: G. Lube, Mathematics Department, NAM, Georg-August University Göttingen, D-37083 Göttingen, Germany.
†E-mail: lube@math.uni-goettingen.de

(URANS) equations (e.g. k–ε, k–ω, RNG–k–ε, SST, etc.). On the one hand, from an engineering point of view, such simulations provide sufficiently good results and have been reaching more and more maturity as a general predictive tool for the design of heating and ventilation systems; but on the other hand, there exist a couple of theoretical drawbacks and it is well known that for certain flow situations URANS models give poor predictions. It would be desirable to use approaches that are closer to the physics of turbulent flows such as large eddy simulation (LES) or variational multiscale methods. Unfortunately, LES calculations are presently still too expensive even for low-turbulence flows. Presently, free convection problems can be simulated only for Rayleigh numbers up to 10^9 [1]. As indoor air flow simulations typically require long-time integration over several hours or even days, this cannot be accomplished using the very small time step size required in an LES. Moreover, there is a growing demand for relatively fast flow solutions, as the flow solver is used more and more as part of an optimization tool. For these reasons, URANS-based simulations will still be relevant in the near future.

In this paper, the transient calculation is based on the k–ε-turbulence model [2] or on improved variants of k–ε–$\overline{v^2}$–f type [3–6], see Section 2. Then, in Section 3, the model is first discretized in time using backward-differencing schemes and then linearized using a Newton-type method per time step. Here, particular attention has to be paid to the proper calculation of (non-negative) turbulence quantities, following ideas of [7–9].

The auxiliary problems of Oseen type and of advection–diffusion–reaction type resulting from the approach in Section 3 are solved using stabilized finite element methods (FEM) of residual type. A major part of the paper, see Section 4, is devoted to the presentation of our recent results in the numerical analysis of these methods [10, 11]. These papers address the application of higher-order methods and of shock-capturing techniques. The numerical solution to the model in boundary layer regions is obtained using either improved wall functions [12, 13] if the k–ε model is used or a hybrid mesh with anisotropic refinement if the $\overline{v^2}-f$ model is applied. Our recent paper [14] on stabilized FEM on such grids provides some analytical background for the latter approach.

In Section 5, we present some applications to indoor air flow simulation based on the research code ParallelNS in combination with building simulation using TRNSYS [15]. Besides the standard flow quantities, it is possible to calculate quantities such as the age of the air. Such quantities are used to develop criteria for the evaluation of the efficiency of air exchange in a room. The quality of the numerical simulations is demonstrated for typical real-life problems.

This paper is based on a keynote lecture at the 14th International Conference on Finite Elements in Flow Problems in Santa Fe 2007 (given by the first author). As it represents work in progress, the applications in Section 5 are based on the k–ε model with improved wall functions [12, 13] whereas the material of Sections 2–4 describes our recent approach based on k–ε–φ–$\overline{f}$ model with wall layer resolution and higher-order finite elements (FEs).

Notation: For a domain G, the norms of the standard Sobolev spaces $W^{k,p}(G)$ with $k \in \mathbb{N}_0$, $p \in [1, \infty]$ are denoted by $\|\cdot\|_{W^{k,p}(G)}$. The $L^2(G)$ norm and the $L^2(G)$ scalar product are denoted by $\|\cdot\|_G$ and $(\cdot,\cdot)_G$.

2. MATHEMATICAL MODEL

Let $\Omega \subset \mathbb{R}^d$, $d = 2, 3$, be a bounded polyhedral domain. The basic mathematical problem in this paper is the (non-dimensional) non-isothermal, incompressible Navier–Stokes model. Buoyancy

DOI: 10.1002/fld

forces are taken into account using the Boussinesq approximation. One seeks the velocity field $\mathbf{u}$, pressure p and temperature θ in $(0,T)\times\Omega$ as solution to the coupled nonlinear system:

$$\partial_t \mathbf{u} - \nabla\cdot(2\nu S(\mathbf{u})) + (\mathbf{u}\cdot\nabla)\mathbf{u} + \nabla p = -\beta\theta\mathbf{g} \tag{1}$$

$$\nabla\cdot\mathbf{u} = 0 \tag{2}$$

$$\partial_t \theta - \nabla\cdot(a\nabla\theta) + (\mathbf{u}\cdot\nabla)\theta = c_p^{-1}\dot{q}^V \tag{3}$$

with the rate of strain tensor $S(\mathbf{u}) = \frac{1}{2}(\nabla\mathbf{u} + \nabla\mathbf{u}^{\mathrm{T}})$, the isobaric volume expansion coefficient β, the gravitational acceleration $\mathbf{g}$, the volumetric heat source $\dot{q}^V$ and the specific heat capacity c_p at constant pressure [16]. The parameters ν and a are the kinematic viscosity and the thermal diffusivity, respectively. The Prandtl number $Pr = \nu/a$ is set to be 0.7 for air flow. The Boussinesq approximation $-\beta\theta\mathbf{g}$ in (1) is applicable if the characteristic temperature difference $\Delta\theta$ is not too large. Otherwise, a more sophisticated model has to be used, e.g. a low-speed compressible flow model, e.g. [17, 18]. Results about existence and uniqueness of solutions to model (1)–(3) can be found in [19, 20]. Results on FEM for the laminar model are given in [19, 21, 22].

Turbulence may occur for large Rayleigh numbers $Ra = \beta|g|L^3\Delta\theta/(\nu a)$ with a characteristic length L, e.g. for natural flow in a closed two-dimensional cavity for $Ra \gtrsim 10^8 \ldots 10^9$. In this paper, statistical turbulence models based on the URANS equations will be considered:

$$\partial_t \mathbf{u} - \nabla\cdot(2\nu_{\mathrm{e}} S(\mathbf{u})) + (\mathbf{u}\cdot\nabla)\mathbf{u} + \nabla p = -\beta\theta\mathbf{g} \tag{4}$$

$$\nabla\cdot\mathbf{u} = 0 \tag{5}$$

$$\partial_t \theta - \nabla\cdot(a_{\mathrm{e}}\nabla\theta) + (\mathbf{u}\cdot\nabla)\theta = c_p^{-1}\dot{q}^V \tag{6}$$

where the averaged values of the unknowns are again denoted by $\mathbf{u}$, p and θ. An eddy viscosity assumption for turbulent effects is considered

$$\nu_{\mathrm{e}} = \nu + \nu_t, \quad a_{\mathrm{e}} = a + \frac{\nu_t}{Pr_t} \tag{7}$$

with $Pr_t = 0.9$ for air. For the turbulent viscosity ν_t, we will use either the standard k–ε model with the turbulent kinetic energy k and the turbulent dissipation rate ε, together with wall functions [7, 9, 13] or, as an improved variant, the k–ε–$\overline{v^2}$–f model with the additionally modelled wall-normal velocity fluctuation $\overline{v^2}$ and the elliptic relaxation f of Durbin and Petterson Reif [4]. More precisely, we will consider the 'code-friendly' φ–$\overline{f}$ version of the k–ε–$\overline{v^2}$–f model [5, 6], the so-called k–ε–φ–$\overline{f}$ model with the additional variable $\varphi = \overline{v^2}/k$ with the turbulent viscosities

$$\nu_t = C_\mu T k\varphi, \quad \nu_k = \nu + \frac{\nu_t}{Pr_k}, \quad \nu_\varepsilon = \nu + \frac{\nu_t}{Pr_\varepsilon} \tag{8}$$

given by

$$\partial_t k - \nabla\cdot(\nu_k\nabla k) + (\mathbf{u}\cdot\nabla)k = P_k + G - \varepsilon \tag{9}$$

$$\partial_t \varepsilon - \nabla\cdot(\nu_\varepsilon\nabla\varepsilon) + (\mathbf{u}\cdot\nabla)\varepsilon + \frac{C_{\varepsilon 2}}{T}\varepsilon = \frac{C_{\varepsilon 1}}{T}(P_k + G) \tag{10}$$

$$\partial_t \varphi - \nabla\cdot(\nu_k\nabla\varphi) + (\mathbf{u}\cdot\nabla)\varphi + \frac{P_k + G}{k}\varphi = \overline{f} + \frac{2\nu_k}{k}\nabla\varphi\cdot\nabla k \tag{11}$$

DOI: 10.1002/fld

and

$$-L^2\Delta\overline{f}+\overline{f}=\frac{(D_1-1)(\frac{2}{3}-\varphi)}{T}+\frac{D_2(P_k+G)}{k}+\frac{2\nu}{k}\nabla\varphi\cdot\nabla k+\nu\Delta\varphi \tag{12}$$

with the turbulent time scale

$$T=\max\left[\min\left(\frac{k}{\varepsilon};\frac{\alpha_r}{C_\mu\sqrt{6}\varphi|S(\mathbf{u})|}\right);6\sqrt{\frac{\nu}{\varepsilon}}\right] \tag{13}$$

and the constants as in Table I. The turbulence length scale in (12) is given by

$$L=C_L\max\left[\min\left(\frac{k^{3/2}}{\varepsilon};\frac{\alpha_r k^{1/2}}{C_\mu\sqrt{6}\varphi|S(\mathbf{u})|}\right);C_\eta\left(\frac{\nu^3}{\varepsilon}\right)^{1/4}\right] \tag{14}$$

The production terms in (9)–(12) are defined as

$$P_k=2\nu_t|S(\mathbf{u})|^2,\quad G=-\beta c_0\frac{k}{\varepsilon}\sum_{i,j=1}^{d}g_i\left[\frac{2}{3}k\delta_{ij}-\nu_t\left(\frac{\partial u_i}{\partial x_j}+\frac{\partial u_j}{\partial x_i}\right)\right]\frac{\partial\theta}{\partial x_j} \tag{15}$$

with $c_0=0.18$ and the components of the gravitational vector g_i. In the definition of G, the so-called generalized gradient-diffusion hypothesis is used, see [3].

The boundary $\partial\Omega$ is split into $\Gamma_-(\mathbf{u})$, $\Gamma_+(\mathbf{u})$ and $\Gamma_W=\Gamma_0(\mathbf{u})$ depending on $\text{sign}(\mathbf{n}\cdot\mathbf{u})$ with the outward pointing unit normal vector $\mathbf{n}$. The k–ε–φ–$\overline{f}$ model is valid down to walls Γ_W of the domain Ω (with exception of the ε-equation) and requires a resolution of the boundary layer region Ω_δ with a layer-adapted grid. Table II contains the boundary conditions where we used the notation $\sigma=2\nu_e S(\mathbf{u})-(p+2/3k)I$. $\Gamma_{W+\delta}$ refers to an artificial boundary with distance δ to Γ_W.

In Section 5, the standard k–ε model will still be applied. It may be considered as special case of the k–ε–φ–$\overline{f}$ model by setting $\nu_t=C_\nu k^2/\varepsilon$ and skipping the equations for φ and $\overline{f}$. Whereas results about existence of solutions to the k–ε–φ–$\overline{f}$ model are not available in the literature, some results about the k–ε approach can be found in [2] and the literature given there.

Table I. Constants of the turbulence model.

$C_{\varepsilon 1}$	$C_{\varepsilon 2}$	C_μ	Pr_k	Pr_ε	D_1	D_2	C_L	C_η	Pr_t	α_r
$1.4(1+0.05\sqrt{1/\varphi})$	1.9	0.22	1.0	1.3	1.4	0.3	0.25	110	0.9	1.0

Table II. Boundary conditions for the k–ε–φ–$\overline{f}$ model.

	Inlet Γ_-	Wall $\Gamma_0=\Gamma_W$ or on $\Gamma_{W+\delta}$	Outlet Γ_+
$\mathbf{u}, p$	$\mathbf{u}=\mathbf{u}_{in}$ or $\sigma\cdot\mathbf{n}=\sigma_n\mathbf{n}$	$\mathbf{u}=\mathbf{0}$	$\sigma\cdot\mathbf{n}=0$
θ	$\theta=\theta_{in}$	$\theta=\theta_W$	$\nabla\theta\cdot\mathbf{n}=0$
k	$k=\frac{3}{2}(T_u\|\mathbf{u}\|)^2$	$k=0$	$\nabla k\cdot\mathbf{n}=0$
ε	$\varepsilon=c_\mu^{3/4}k^{3/2}/L$	$\varepsilon=\frac{2\nu}{\delta^2}k_\delta$ on $\Gamma_{W+\delta}$	$\nabla\varepsilon\cdot\mathbf{n}=0$
φ	$\varphi=\frac{2}{3}$	$\varphi=0$	$\nabla\varphi\cdot\mathbf{n}=0$
$\overline{f}$	$\nabla\overline{f}\cdot\mathbf{n}=0$	$\overline{f}=0$	$\nabla\overline{f}\cdot\mathbf{n}=0$

DOI: 10.1002/fld

For the standard k–ε model, an improved wall function method is employed at the Dirichlet walls [12, 13], where modified boundary conditions are used prescribing the wall-shear stress $\boldsymbol{\tau}_{\mathrm{w}}$ and the heat flux $\dot{q}$:

$$\mathbf{u}\cdot\mathbf{n}=0, \quad (\mathbb{I}-\mathbf{n}\otimes\mathbf{n})\sigma\mathbf{n}=\boldsymbol{\tau}_{\mathrm{w}} \tag{16}$$

$$a_{\mathrm{e}}\nabla\theta\cdot\mathbf{n}=\dot{q}c_p^{-1} \tag{17}$$

Therein, $\boldsymbol{\tau}_{\mathrm{w}}$ and $\dot{q}$ are obtained from the integration of the one-dimensional boundary layer equations in the near-wall region where an algebraic turbulence model designed for buoyancy-driven flows is used.

3. TIME DISCRETIZATION, LINEARIZATION AND DECOUPLING

The highly nonlinear coupled system (4)–(15) as described in the previous section requires a proper time discretization, linearization and decoupling.

For the time discretization of the non-isothermal Navier–Stokes block (4)–(6), a linearized backward-differencing scheme BDF(2) is applied with

$$\partial_t\theta|_{t=t_m}\approx\frac{3\theta^m-4\theta^{m-1}+\theta^{m-2}}{2\Delta t_m}$$

and $\theta^m=\theta|_{t=t_m}$. Similar notation is used for the other time derivatives. Setting

$$\mathbf{U}^m=2\mathbf{u}^{m-1}-\mathbf{u}^{m-2}, \quad T^m=2\theta^{m-1}-\theta^{m-2}$$

the semidiscrete form of the non-isothermal Navier–Stokes block reads

$$-\nabla\cdot(2\nu_{\mathrm{e}}^m S(\mathbf{u}^m))+(\mathbf{U}^m\cdot\nabla)\mathbf{u}^m+\frac{3\mathbf{u}^m}{2\Delta t_m}+\nabla p^m=-\beta T^m\mathbf{g}+\frac{4\mathbf{u}^{m-1}-\mathbf{u}^{m-2}}{2\Delta t_m}$$

$$\nabla\cdot\mathbf{u}^m=0$$

$$-\nabla\cdot(a_{\mathrm{e}}^m\nabla\theta^m)+(\mathbf{U}^m\cdot\nabla)\theta^m+\frac{3}{2\Delta t_m}\theta^m=\frac{1}{c_p}\dot{q}^{V\,m}+\frac{4\theta^{m-1}-\theta^{m-2}}{2\Delta t_m}$$

The analysis of the linearized and nonlinear BDF(2) schemes for the laminar, isothermal Navier–Stokes model has been considered in [23]. For the nonlinear variant and constant time steps Δt_m, one obtains a rate of $0(\tau^2)$ for the time-averaged velocity error in $l^2(H^1(\Omega))\cap l^\infty(L^2(\Omega))$ and of $0(\tau)$ for the time-averaged pressure error in $l^\infty(L^2(\Omega)/\mathbb{R})$. For the linearized variant as above, one eventually obtains an order reduction. The analysis of the BDF(2) scheme with variable time steps is open so far. In particular, stability problems may occur for increasing time steps.

Next, the turbulence block (9)–(12) of the k–ε–φ–$\overline{f}$ model is a strongly coupled, nonlinear system of advection–diffusion–reaction equations. A major problem is a positivity-preserving formulation for k,ε,φ and $\overline{f}$. One possibility is to modify the nonlinear iteration approach by [7–9] given for the standard k–ε scheme. Consider for simplicity, the k-equation

$$\partial_t k-\nabla\cdot(\nu_k\nabla k)+(\mathbf{u}\cdot\nabla)k+\frac{\varepsilon}{k}k=P_k+G$$

DOI: 10.1002/fld

In one step of the linearization loop, the non-negative reaction coefficient ε/k, the diffusion coefficients ν_k and the right-hand side P_k+G are 'frozen'. In order to preserve a (continuous) maximum principle for the linearized problems, one can replace these terms by $\max(\varepsilon/k;0)$, etc. Note that the maximum principle for the linearized equation will be preserved after semidiscretization with BDF(2). As the maximum principle does not automatically transfer to the problem after discretization in space, another (crosswind type) stabilization will be introduced later on in Section 4.

The linearization cycle within each BDF(2) time step is formally given as follows:

(A) Solve the semidiscretized non-isothermal Navier–Stokes equations using a block Gauss–Seidel-type method with iterative decoupling of the equations:

- Update the turbulent viscosity ν_t^m and the turbulent thermal diffusivity a_t^m.
- Solve the linearized Navier–Stokes problem for $\mathbf{u}^m$, p^m.
- Solve the linearized advection–diffusion–reaction problem for θ^m.

(B) Solve the semidiscretized equations for the turbulence quantities using a block Gauss–Seidel-type method with iterative decoupling of the equations:

- Update the non-negative reaction and diffusion coefficients and right-hand sides.
- Solve for $k^m, \varepsilon^m, \varphi^m, \overline{f}^m$ (until convergence).

(C) Stopping criterion: Go to (A) if some stopping criteria for $\mathbf{u}^m$, p^m, θ^m are not yet fulfilled. Otherwise go to the next time step.

4. RESIDUAL-BASED STABILIZATION OF LINEARIZED SUBPROBLEMS

The iteration scheme (A)–(C) for semidiscretization in time, linearization and decoupling of the k–ε–φ–$\overline{f}$ model leads to linearized auxiliary problems of

- advection–diffusion–reaction type for θ and $k, \varepsilon, \varphi, \overline{f}$;
- Oseen type for $\mathbf{u}$, p.

In this section, recent results for a proper stabilized FE discretization of these schemes will be summarized and discussed. For the efficient solution to the arising algebraic problems, the reader is referred to the presentation in [24, 25]. In particular, the parallelization via a non-overlapping domain decomposition together with optimized interface conditions of Robin type between the subdomains is proposed.

4.1. Linearized advection–diffusion–reaction model on isotropic meshes

Consider first for $u\in\{\theta, k, \varepsilon, \varphi, \overline{f}\}$ the linearized advection–diffusion–reaction model

$$Lu := -\nabla\cdot(a\nabla u)+(\mathbf{b}\cdot\nabla)u+cu=f \ \text{ in } \Omega, \quad u=0 \ \text{ on } \partial\Omega \tag{18}$$

with coefficients $a, c\in L^\infty(\Omega)$, $\mathbf{b}\in(H^1(\Omega))^d\cap(L^\infty(\Omega))^d$ and source term $f\in L^2(\Omega)$. Note that the application of turbulence models in Sections 2 and 3 requires a variable diffusion coefficient a. The boundary condition is prescribed only for ease of presentation. Moreover, assume

$$a(x)\geqslant a_0>0, \quad (\nabla\cdot\mathbf{b})(x)=0, \quad c(x)\geqslant 0 \quad \text{a.e. in } \Omega$$

DOI: 10.1002/fld

The coefficient c is normally given as the sum of a reaction term $\tilde{c}$ and an inverse time step $1/\Delta t$. The basic variational formulation of (18) reads

$$\text{Find } u \in V := H_0^1(\Omega) \quad \text{s.t. } A(u, v) = l(v) \quad \forall v \in V \tag{19}$$

with

$$A(u, v) := (a\nabla u, \nabla v)_\Omega + (\mathbf{b}\cdot\nabla u + cu, v)_\Omega \tag{20}$$

$$l(v) := (f, v)_\Omega \tag{21}$$

Let $\mathscr{T}_h$ be an admissible triangulation of the polyhedral domain Ω consisting of shape-regular (isotropic) elements. $V_h := \{v \in H_0^1(\Omega) \cap C(\bar{\Omega}) | v|_T \in P_r(T) \forall T \in \mathscr{T}_h\}$ is a conforming FE subspace. We apply a modified streamline-upwind/Petrov–Galerkin (SUPG) scheme

$$\text{Find } u \in V_h: \ A_{\text{rbs}}(u, v) = L_{\text{rbs}}(v) \quad \forall v \in V_h \tag{22}$$

with

$$A_{\text{rbs}}(u, v) := (a\nabla u, \nabla v)_\Omega + (\mathbf{b}\cdot\nabla u + cu, v)_\Omega + \sum_{T\in\mathscr{T}_h} \delta_T (\hat{L}u, \mathbf{b}\cdot\nabla v)_T \tag{23}$$

$$L_{\text{rbs}}(v) := (f, v)_\Omega + \sum_{T\in\mathscr{T}_h} \delta_T (f, \mathbf{b}\cdot\nabla v)_T \tag{24}$$

In order to treat the variable diffusion coefficient a, the modified elliptic operator

$$\hat{L}u|_T := -\nabla\cdot\Pi_T(a\nabla u) + (\mathbf{b}\cdot\nabla)u + cu \tag{25}$$

together with the L^2-orthogonal projection $\Pi_T : [L^2(T)]^d \to [P_r(T)]^d$ is introduced.

The analysis of this SUPG-FEM is performed with respect to the following triple norm

$$|||v||| := \left(\sum_{T\in\mathscr{T}_h} (\|\sqrt{a}\nabla v\|^2_{(L^2(T))^d} + \|\sqrt{c}v\|^2_{L^2(T)} + \delta_T \|\mathbf{b}\cdot\nabla v\|^2_{L^2(T)}) \right)^{1/2}$$

Theorem 1 (*Lube and Rapin* [*11*])
Let the set $\{\delta_T\}$ of SUPG parameters be chosen as

$$\delta_T \sim \min\left\{ \frac{h_T}{r\|\mathbf{b}\|_{(L^\infty(T))^d}}; \frac{1}{\|c\|_{L^\infty(T)}}; \frac{h_T^2}{r^4\|a\|_{L^\infty(T)}} \right\} \tag{26}$$

Then the discrete problem (22) admits a unique solution $u_h \in V_h$ and the *a priori* error estimate:

$$|||u - u_h|||^2 \leqslant C \sum_{T\in\mathscr{T}_h} \frac{h_T^{2(l-1)}}{r^{2(k-1)}} M_T^{\text{opt}} \|u\|^2_{H^k(T)}, \quad l = \min(r+1, k) \tag{27}$$

with

$$M_T^{\text{opt}} := \|a\|_{L^\infty(T)} \left(1 + Pe_T + \Gamma_T + \min\left(\frac{\|a\|_{L^\infty(T)}}{\inf_T a} Pe_T^2; r^2 \right) + \frac{\|a\|^2_{W^{k-1,\infty}(T)}}{\|a\|^2_{L^\infty(T)}} \right) \tag{28}$$

DOI: 10.1002/fld

and

$$Pe_T := \frac{h_T \|\mathbf{b}\|_{(L^\infty(T))^d}}{r\|a\|_{L^\infty(T)}}, \quad \Gamma_T := \frac{\|c\|_{L^\infty(T)} h_T^2}{r^2 \|a\|_{L^\infty(T)}} \tag{29}$$

The proof is based on the stability estimate $A_{\mathrm{rbs}}(v,v) \geqslant \frac{1}{2}|||v|||^2$ for all $v \in V_h$ and a modified Galerkin orthogonality condition stemming from the modification (25). The *a priori* estimate (27)–(29) reflects the influence of the polynomial degree r and of the variable viscosity coefficient a. The latter fact is essential for the RANS-based turbulence model.

For a two-dimensional advection–diffusion–reaction problem with an a-independent smooth solution, Figure 1 shows the remarkable effect of an increasing polynomial degree for fixed mesh sizes h. The result is valid for vanishing and large reaction terms, which may correspond to an infinite or small time step Δt.

Besides the *a priori* error estimate in Theorem 1, *a posteriori* estimates can be applied to scheme (22) with the goal of adaptive spatial mesh refinement, see, e.g. [26].

It is well known that the SUPG solution may suffer from spurious local oscillations in shear layers. This is, in particular, very dangerous for the solutions to advection–diffusion–reaction problems for the turbulence quantities as they have to be non-negative. As a remedy, the following class of crosswind-stabilized (cs) variants of the SUPG scheme are considered as

$$\text{Find } u_h \in V_h: \; A_{\mathrm{rbs}}(u_h, v) + \sum_{T \in \mathscr{T}_h} (\tau_T^{\mathrm{cs}}(u_h) D_{\mathrm{cs}} \nabla u_h, \nabla v)_T = L_{\mathrm{rbs}}(v) \quad \forall v \in V_h \tag{30}$$

with

$$D_{\mathrm{cs}} := \begin{cases} I - \dfrac{\mathbf{b}\otimes\mathbf{b}}{|\mathbf{b}|^2}, & \mathbf{b} \neq 0 \\ 0, & \mathbf{b} = 0 \end{cases}, \quad \tau_T^{\mathrm{cs}}(w) := l_T^{\mathrm{cs}}(w) \underbrace{\frac{\|\hat{L}w - f\|_{L^2(T)}}{|w|_{H^1(T)} + \kappa_T}}_{=: R_T^*(w)} \tag{31}$$

and a very small term $\kappa_T > 0$.

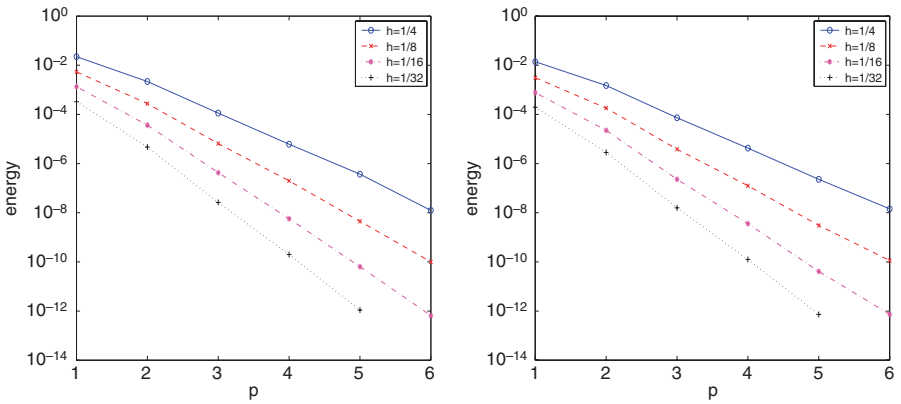

Figure 1. Convergence w.r.t. the polynomial order p in the triple norm $|||u - u_h|||$ for fixed (isotropic) mesh width h for $a = 10^{-6}, c = 0$ (left) and $a = 10^{-6}, c = 10^3$ (right).

DOI: 10.1002/fld

Theorem 2 (*Lube and Rapin* [*11*])
Choose δ_T as in (26). Let the restriction $0 \leqslant l_T^{\mathrm{cs}}(w) \leqslant \rho \delta_T R_T^*(w)$ for all $w \in V_h$ with appropriate $\rho > 0$ on the limiter function be valid. Moreover, let the solution to (18) be smooth such that $(\nabla \cdot (a \nabla u))|_T \in L^2(T)$ and $u \in H^k(T)$, $k > d/2$ for all $T \in \mathscr{T}_h$. Then the solution u_h to the crosswind-stabilized SUPG scheme (30)–(31) admits the error estimate

$$|||u-u_h|||^2 + \sum_{T \in \mathscr{T}_h} \|(\tau_T^{\mathrm{cs}}(u_h) D_{\mathrm{cs}}^{\mathrm{cd}})^{1/2} \nabla (u-u_h)\|_{(L^2(T))^d}^2 \leqslant C \sum_{T \in \mathscr{T}_h} \frac{h_T^{2(l-1)}}{r^{2(k-1)}} M_T^{\mathrm{opt}} \|u\|_{H^k(T)}^2 \tag{32}$$

The estimate (32) provides additional control of the crosswind-stabilization term without degrading the right-hand side of estimate (27)–(29) for the basic SUPG scheme (22)–(25). The result gives only an upper bound of the limiter function $l_T^{\mathrm{cs}}(\cdot)$; hence, other analytical tools are necessary for its design. In particular, the discontinuity-capturing/crosswind-dissipation (DC/CD) scheme [7] with the limiter function

$$l_T^{\mathrm{cd}}(w) = l_T^{\mathrm{dc/cd}}(w) := \frac{1}{2} h_T \max\left\{0, \beta - \frac{2\|a\|_{L^\infty(T)}}{h_T R_T^*(w)}\right\}, \quad \kappa_T = 0 \tag{33}$$

can be used within the framework of crosswind-stabilized SUPG schemes for appropriate values of β. Consider a problem with an interior layer skew to the mesh in $\Omega = (0,1)^2$ with the solution $u(x) = 1/2(1 - \tanh((2x_1 - x_2 - 1/4)/\sqrt{5a})$ and data $a = 10^{-6}$, $\mathbf{b}(x) = 1/\sqrt{5}(1,2)^T$, $c = 0$, $f = Lu$. In Figure 2, the SUPG-FEM without and with the DC/CD scheme [7] using the choice (33) are compared. Note that the crosswind stabilization preserves the steep gradient of the SUPG scheme. Again, a remarkable improvement is observed for increasing polynomial degree and fixed (isotropic) mesh size h.

A serious problem appears in the treatment of the corresponding nonlinear algebraic problems if the stationary case is considered. A convenient approach is a semi-implicit treatment of the nonlinearity within linearization loop (A)–(C).

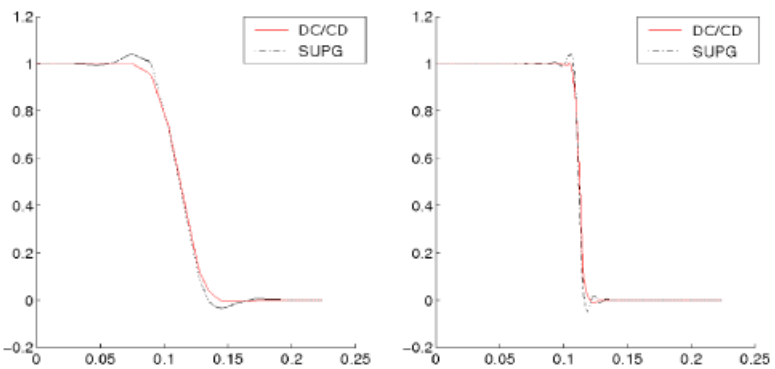

Figure 2. SUPG-FEM without/with DC/CD for $h = \frac{1}{64}$, $r \in \{1, 4\}$, $\beta = 0.7$, $\kappa = 10^{-4}$.

DOI: 10.1002/fld

4.2. Linearized incompressible problems of Oseen type on isotropic meshes

Consider now a linearized incompressible problem of Oseen type

$$-\nabla\cdot(2\nu S(\mathbf{u}))+(\mathbf{b}\cdot\nabla)\mathbf{u}+c\mathbf{u}+\nabla p=\mathbf{f} \quad \text{in } \Omega \tag{34}$$

$$\nabla\cdot\mathbf{u}=0 \quad \text{in } \Omega \tag{35}$$

$$\mathbf{u}=\mathbf{0} \quad \text{on } \partial\Omega \tag{36}$$

with

$$\nu(x)\geqslant\nu_0>0, \quad (\nabla\cdot\mathbf{b})(x)=0, \quad \frac{1}{\Delta t}\sim c=\text{const.}\geqslant 0 \quad \text{a.e. in } \Omega$$

Again, no-slip conditions (36) are prescribed for ease of presentation. Using the spaces $\mathbf{W}:=\mathbf{V}\times\mathbf{Q}:=(H_0^1(\Omega))^d\times L_0^2(\Omega)$, the variational formulation of problem (34)–(36) reads

$$\text{find } U=\{\mathbf{u},p\}\in\mathbf{W} \quad \text{s.t. } \mathscr{A}(\mathbf{b};U,V)=\mathscr{L}(V) \ \ \forall V=\{\mathbf{v},q\}\in\mathbf{W} \tag{37}$$

with

$$\mathscr{A}(\mathbf{b};U,V):=(2\nu S(\mathbf{u}),\nabla\mathbf{v})_\Omega+((\mathbf{b}\cdot\nabla)\mathbf{u}+c\mathbf{u},\mathbf{v})_\Omega-(p,\nabla\cdot\mathbf{v})_\Omega+(q,\nabla\cdot\mathbf{u})_\Omega \tag{38}$$

$$\mathscr{L}(V):=(\mathbf{f},\mathbf{v})_\Omega \tag{39}$$

We consider an admissible and shape-regular (isotropic) triangulation $\mathscr{T}_h$ of the polyhedral domain Ω and the FE subspaces

$$X_h^r:=\{v\in C(\bar{\Omega})\,|\,v|_T\in P_r(T)\forall T\in\mathscr{T}_h\}, \quad r\in\mathbf{N}$$

It is well known that equal-order FE spaces for velocity/pressure

$$\mathbf{W}_h^{r,r}:=\mathbf{V}_h^r\times\mathbf{Q}_h^r:=[X_h^r\cap H_0^1(\Omega)]^d\times(X_h^r\cap L_0^2(\Omega))$$

violate the discrete inf–sup (or Babuska–Brezzi) stability condition. As a consequence, the basic Galerkin FEM

$$\text{find } U=\{\mathbf{u},p\}\in\mathbf{W}_h^{r,r} \quad \text{s.t. } \mathscr{A}(\mathbf{b};U,V)=\mathscr{L}(V) \ \ \forall V=\{\mathbf{v},q\}\in\mathbf{W}_h^{r,r}$$

may suffer from spurious pressure oscillations. Another source of instabilities may occur if the advection term dominates the diffusion terms. As a remedy, the following 'classical' residual-based scheme is considered:

$$\text{find } U=\{\mathbf{u},p\}\in\mathbf{W}_h^{r,r}:\mathscr{A}_{\text{rbs}}(\mathbf{b};U,V)=\mathscr{L}_{\text{rbs}}(V) \quad \forall V=\{\mathbf{v},q\}\in\mathbf{W}_h^{r,r} \tag{40}$$

with

$$\mathscr{A}_{\text{rbs}}(\mathbf{b};U,V)=\mathscr{A}(\mathbf{b};U,V)+\sum_T\underbrace{\delta_T(\hat{L}_{Os}(\mathbf{b};\mathbf{u},p),(\mathbf{b}\cdot\nabla)\mathbf{v}+\nabla q)_T}_{\text{SUPG- and PSPG-stabilization}}+\underbrace{\gamma_T(\nabla\cdot\mathbf{u},\nabla\cdot\mathbf{v})_T}_{\text{div-stabilization}} \tag{41}$$

$$\mathscr{L}_{\text{rbs}}(V)=\mathscr{L}(V)+\sum_T\overbrace{\delta_T(\mathbf{f},(\mathbf{b}\cdot\nabla)\mathbf{v}+\nabla q)_T} \tag{42}$$

DOI: 10.1002/fld

PSPG stabilization stands for pressure stabilization/Petrov–Galerkin stabilization. The case of variable viscosity v appearing in the turbulent case is treated by

$$\hat{L}_{Os}(\mathbf{b};\mathbf{u},p) := -\nabla\cdot\Pi_T(2vS(\mathbf{u})) + \nabla p + (\mathbf{b}\cdot\nabla)\mathbf{u} + c\mathbf{u} \tag{43}$$

with the orthogonal L^2-projection $\Pi_T : [L^2(T)]^{d\times d} \to [P_r(T)]^{d\times d}$.

The analysis of scheme (40)–(43) on isotropic meshes is performed with respect to the following triple norm $|[\cdot]|_{\mathrm{rbs}}$ according to

$$|[V]|_{\mathrm{rbs}}{}^2 := \|\sqrt{2v}S(\mathbf{v})\|^2_{L^2(\Omega)} + \|\sqrt{c}\mathbf{v}\|^2_{L^2(\Omega)} + \sum_T (\delta_T \|(\mathbf{b}\cdot\nabla)\mathbf{v} + \nabla q\|^2_{L^2(T)} + \gamma_T \|\nabla\cdot\mathbf{v}\|^2_{L^2(T)})$$

and leads to the following result.

Theorem 3 (*Lube and Rapin* [*10*])
Let the SUPG/PSPG parameters $\{\delta_T\}$ and parameters $\{\gamma_T\}$ be chosen as

$$\delta_T \sim \min\left\{\frac{h_T^2}{r^2\|v\|_{L^\infty(T)}}; \frac{1}{\|c\|_{L^\infty(T)}}; \frac{h_T}{r\|\mathbf{b}\|_{(L^\infty(T))^d}}\right\}, \quad \gamma_T \sim \frac{h_T^2}{r^2\delta_T} \tag{44}$$

Then the discrete problem (40)–(43) admits a unique solution $U_h = \{\mathbf{u}_h, p_h\} \in \mathbf{W}_h^{r,r}$ and the *a priori* error estimate

$$\begin{aligned} |[U-U_h]|^2_{\mathrm{rbs}} \leqslant C \sum_{T\in\mathscr{T}_h} \frac{h_T^{2(l-1)}}{r^{2(k-1)}} (\|\mathbf{u}\|^2_{H^k(T)} + \|p\|^2_{H^k(T)}) \\ \times \left(\|v\|_{L^\infty(T)} + \frac{\|v\|^2_{W^{k-1,\infty}(T)}}{\|v\|_{L^\infty(T)}} + \frac{\|\mathbf{b}\|_{(L^\infty(T))^d} h_T}{r} + \frac{\|c\|_{L^\infty(T)} h_T^2}{r^2}\right) \end{aligned} \tag{45}$$

The proof basically relies on the stability condition $\mathscr{A}_{\mathrm{rbs}}(\mathbf{b};V,V) \geqslant \frac{1}{2}|[V]|^2_{\mathrm{rbs}}, \forall V = \{\mathbf{v},q\} \in \mathbf{V}_h^r \times \mathbf{Q}_h^r$. The result is a proper extension of Theorem 1. Note that additionally a weighted L^2-error estimate for the pressure can be given, see [10].

In Figure 3 we present the r-convergence of the equal-order scheme (40)–(43) for a smooth and v-independent solution for $v = 10^{-6}, c = 0$ for some fixed isotropic mesh sizes h.

Note that the application of *a posteriori* techniques can be used for a proper adaptive refinement of the spatial mesh, see, e.g. [27].

4.3. Residual-based stabilization on hybrid meshes

The efficient resolution of boundary layers at a wall Γ_W can be accomplished using an anisotropic refinement of the layer region. Consider the special situation of a shear layer being located at a wall (here at $x_d = 0$). A boundary-fitted hybrid mesh $\mathscr{T}_h = \mathscr{T}_h^g \cup \mathscr{T}_h^{bl}$ consists of an (unstructured) isotropic mesh $\mathscr{T}_h^g$ away from wall layers and a structured anisotropic mesh $\mathscr{T}_h^{bl}$ of the so-called tensor product type [28], see Figure 4.

The analysis of the residual-based stabilized scheme of Section 4.2 on shape-regular (isotropic) meshes has been extended in [14] to this idealized situation. Assume that the tensor-product-type

DOI: 10.1002/fld

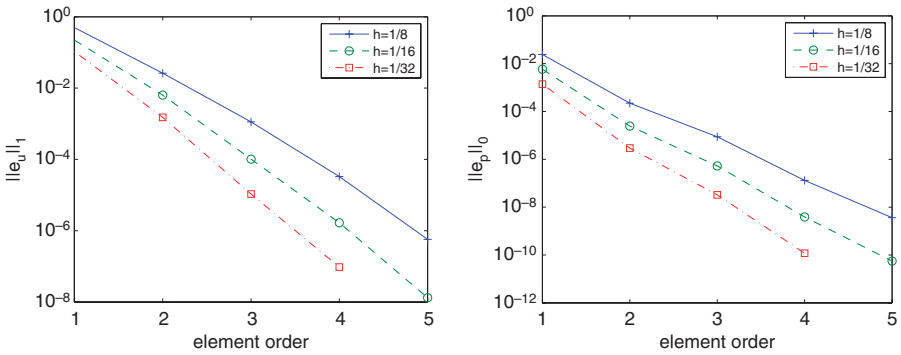

Figure 3. Convergence w.r.t. the polynomial order for smooth solution with $\nu = 10^{-6}, c = 0$ and fixed h: $\|\nabla(\mathbf{u} - \mathbf{u}_h)\|_0$ (left), $\|p - p_h\|_0$ (right).

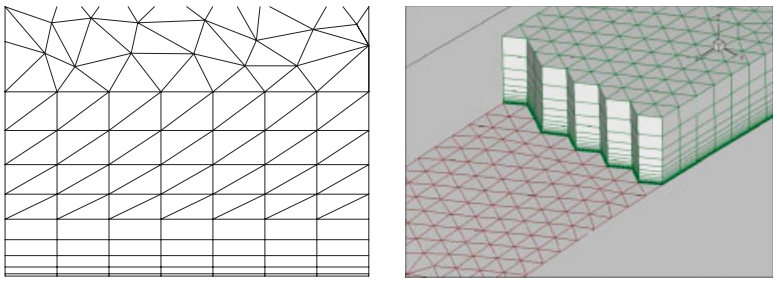

Figure 4. Examples of hybrid meshes for $d = 2$ and 3.

mesh in the layer zone is refined in the x_d-direction towards the wall such that the aspect ratio of the elements nearest to the wall at $x_d = 0$ behaves like

$$\frac{h_{\max,T}}{h_{\min,T}} \sim \frac{1}{\text{characteristic length scale}} \tag{46}$$

For a laminar channel flow, the 'characteristic length scale' is of order $\sqrt{\nu}$ for unit channel height. For turbulent channel flow, it typically corresponds to ν/u_τ with friction velocity $u_\tau = \left(\nu \partial u_1/\partial x_2|_{\Gamma_W}\right)^{1/2}$.

Basic ingredients of the analysis in [14] are local (anisotropic) interpolation estimates and a modified design of the stabilization parameters. Suppose for each element T that

$$\delta_T \sim \min\left(\frac{h_{\min,T}^2}{\nu}; \frac{1}{\|c\|_{L^\infty(T)}}; \frac{\tilde{h}_T}{\|\mathbf{b}\|_{(L^\infty(T))^d}}\right), \quad \gamma_T \sim \frac{h_{\max,T}^2}{\delta_T} \tag{47}$$

with a characteristic length $\tilde{h}_T \in [h_{\min,T}, h_{\max,T}]$. In the isotropic region $\mathscr{T}_h^g$, one obtains the standard parameter design (44) setting $\tilde{h}_T \sim h_{\max,T}$. Numerical experience shows that the influence of the length scale $\tilde{h}_T$ is not very critical in the anisotropic region $\mathscr{T}_h^{bl}$. The choice $\tilde{h}_T = \text{vol}(T)^{1/d}$ provides a reasonable compromise between accuracy and computational costs. For an application

DOI: 10.1002/fld

of the approach to the isotropic turbulent channel flow at $Re_\tau = 395$ based on the k–ε–φ–$\overline{f}$ model, we refer to [14]. A very good agreement of the main flow profile and of turbulence quantities to the DNS data of [29] and to numerical results in [5] is obtained.

Note that a similar approach and analysis can be extended to advection–diffusion–reaction problems (18).

4.4. Application to a non-isothermal benchmark problem

The approach presented in Sections 3 and 4 is applied to the non-isothermal turbulent flow in a closed cavity at $Ra = 1.58 \times 10^9$ using the k–ε–φ–$\overline{f}$ model. The cavity has dimension $(0, L)^2 \times (0, b)$ with $L = 0.75\,\mathrm{m}$, $b = 0.04\,\mathrm{m}$ and is filled with air, i.e. $\nu = 1.53 \times 10^{-5}\,\mathrm{m^2\,s^{-1}}$, $a = 2.186 \times 10^{-5}\,\mathrm{m^2\,s^{-1}}$ and $\beta = 3.192 \times 10^{-3}\,\mathrm{K^{-1}}$. The initial conditions are $\mathbf{u}|_{t=0} = \mathbf{0}$, $\theta|_{t=0} = 303.15\,\mathrm{K}$. The sidewalls are held at different temperatures $\theta_w = 323.15\,\mathrm{K}$ for the left hot sidewall and $\theta_w = 283.15\,\mathrm{K}$ for the right cold sidewall. On top and bottom walls θ_w is prescribed using the experimental data of [30]. The boundary conditions in the spanwise direction are designed to simulate symmetry faces. Figure 5 (left) gives some illustration.

The results are simulated on a simplicial mesh with $69 \times 69 \times 5$ nodes in the x_1-, x_2- and x_3-directions. An anisotropic mesh refinement starting with the first grid line at a wall distance of $0.001\,\mathrm{m}$ is used for the x_1- and x_2-directions to resolve the boundary layers, see Figure 5 (right). Piecewise linear elements ($r = 1$) for all unknowns together with all stabilization techniques (as described in this section) are used. The results are compared with experimental data in [30] and with numerical results using the k–ε model with wall functions, see [13].

Figure 6 shows the boundary layer profiles for the vertical velocity component u_2/u_0 (with reference velocity $u_0 = 0.9692\,\mathrm{m\,s^{-1}}$) near the hot left wall at $y/L = 0.2$ and 0.5 for the k–ε–φ–$\overline{f}$ model, which are in reasonable agreement with the experimental data. Regarding the velocity profile at $y/L = 0.2$, it has to be mentioned that the experiment shows the existence of small recirculation regions of low fluid velocity (cf. Figure 9 in [30]), which are difficult to capture in the simulations due to the modelling assumptions of the turbulence models. At $y/L = 0.8$, the deviation of the predicted velocity profile from the experimental data is more pronounced (not shown here), as the growth of the boundary layer thickness along the hot wall in the streamwise direction is underpredicted by the k–ε–φ–$\overline{f}$ model. This will be subject to future research. Figure 7

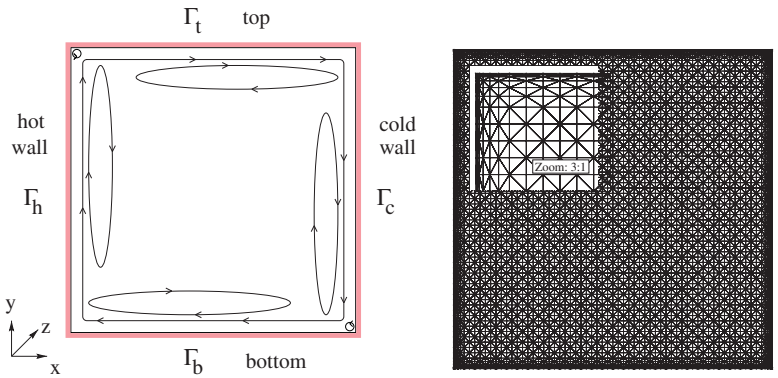

Figure 5. Sketch of cavity and streamlines (left) and of the mesh (right) for closed cavity flow [30].

DOI: 10.1002/fld

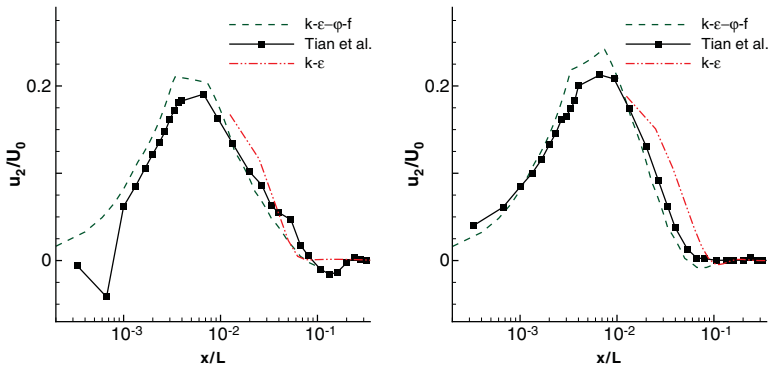

Figure 6. Boundary layer profiles for vertical velocity component u_2/u_0 near hot left wall at $y/L=0.2$ (left) and $y/L=0.5$ (right) and experimental data of [30].

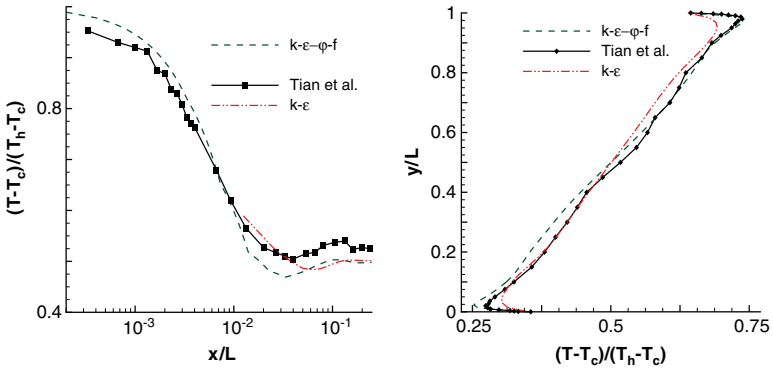

Figure 7. Horizontal temperature profile $(T-T_c)/(T_h-T_c)$ near hot left wall at $y/L=0.5$ (left) and vertical temperature profile $(T-T_c)/(T_h-T_c)$ at $x/L=0.5$.

(left) shows the horizontal temperature profile near the hot wall at $y/L=0.5$ that demonstrates the proper resolution of the temperature boundary layer. For the cold wall, agreement with the experimental data is similar to the corresponding positions at the hot wall. Figure 7 (right) shows the prediction of the vertical gradient of the temperature profile. Near the top wall, the agreement with the experimental data is very good, but in the lower half of the cavity, temperature is predicted too low by the k–ε–φ–$\overline{f}$ model. Such a behaviour was also observed even for a fully resolved LES by [31], who report that the flow in the midsection $x_3=b/2$ exhibits to some extent three-dimensional features if the end walls in the x_3-direction are taken into account.

5. APPLICATION TO INDOOR AIR-FLOW SIMULATION

In this section, recent results for the k–ε URANS model together with modified wall functions are reported. Note that a full resolution of the boundary layers (as for the previous example) is

DOI: 10.1002/fld

currently not feasible for routine indoor air-flow simulations. Within the modified wall treatment, a one-dimensional boundary layer computation on an embedded subgrid between the wall and the first off-wall node is used, see, e.g. [13] for more details and for a validation of the method, which has been demonstrated to be very beneficial for heat transfer calculations. In that way the wall distance of the first subgrid point is lower than 0.003 m, whereas it is 0.05 m for the first grid point of the tetrahedral mesh.

The simulations have been performed on simplicial meshes with piecewise linear elements for all unknowns. The FE meshes contain approximately 200 000–600 000 elements. All stabilization techniques (as described in Section 4) are applied. In particular, the DC/CD scheme is important to avoid non-physical oscillations in the energy equation. The non-linearity of this scheme can be efficiently treated together with the non-linearities of the turbulence model using the described iterative solution scheme.

For many practical simulations, a better resolution of the flow is mandatory. This is in particular true for flows with unsteady separation, which will become more and more important for future applications. The results in Section 4 show that it is much more efficient with respect to the number of unknowns to increase the polynomial order than to refine the mesh. Moreover, using higher-order elements yields much sharper layers and the oscillations in the crosswind direction are considerably smaller, cf. Figure 2.

The implementation of the full k–ε–φ–$\overline{f}$ URANS model with higher-order schemes according to the presentation in Sections 3 and 4 is still work in progress. Corresponding results will be reported elsewhere.

5.1. *Efficiency of ventilation processes*

An important criterion for the evaluation of the indoor air climate is the air-exchange efficiency. It is defined as the ratio ε_a of the minimal residence time τ_n to the doubled averaged residence time $\langle\tau\rangle$, see [32]. By the use of tracer gas techniques, the air-exchange efficiency can be measured in experiments. For computations it is helpful to apply the concept of the age of the air, see also [32]. However, the traditional theory is mainly restricted to stationary situations. Alternatively, one can compute the age of the air τ_p by the transient advection–diffusion problem

$$\frac{\partial \tau_p}{\partial t} + (\mathbf{u}\cdot\nabla)\tau_p - \nabla\cdot(a_{\tau,\mathrm{e}}\nabla\tau_p) = 1 \quad \text{in } \Omega$$

$$\tau_p = \tau_{p,in} \quad \text{on } \Gamma_-(\mathbf{u}), \quad a_{\tau,\mathrm{e}}\nabla\tau_p\cdot\mathbf{n} = 0 \quad \text{on } \Gamma_+(\mathbf{u})\cup\Gamma_W$$

This problem can be treated using the approach proposed in Section 4. Afterwards the local data of the age of the air are available for the evaluation of the ventilation process. In order to assess different situations, it is common to work with a local air-exchange index

$$\varepsilon^a_{p,t} = \frac{\tau^{\mathrm{out}}_{p,\mathrm{ref}}}{\tau_p} \quad \text{with } \tau^{\mathrm{out}}_{p,\mathrm{ref}} = \frac{1}{\int_{\Gamma_+} do}\int_{\Gamma_+}\tau^{\mathrm{ref}}_p \mathrm{d}o$$

via comparison with the idealized displacement flow (piston flow) with the same flow rate $\dot{V} = \int_{\Gamma_-}\mathbf{u}\cdot\mathbf{n}\mathrm{d}o$. Herein $\tau^{\mathrm{out}}_{p,\mathrm{ref}}$ represents the age of the air at the outlet of the reference flow. (Note that the local air-exchange index $\varepsilon^a_{p,t}$ is not defined in the inlet opening.)

In addition to the air-exchange index, it is possible to calculate the air-exchange efficiency for transient situations by generating an idealized reference flow (piston flow) with the same mean

DOI: 10.1002/fld

age of the air. Details are given in [33]. In particular, the stationary criterion given above appears as a special case.

As a first application, Figure 8 (right) presents the isosurfaces of the air-exchange index of an office room during natural ventilation via an opened window (see Figure 8, left). The efficient refreshment of the air in the working area of the office is obvious. For calculating the conditions for the flow through the opening, the above-mentioned domain decomposition method can be applied, see [13].

The next application is a displacement ventilation in a conference room with 'people' around a conference table, see Figure 9. Boundary conditions for the temperature are computed by coupling the CFD code with a thermal building simulation program using PVM [34]. Very reasonable temperatures in the working area of the conference room together with low flow velocities can be obtained from Figure 9. The efficiency of the ventilation according to the working principle of a displacement ventilation system is documented in Figure 9 (right) for a cross section of the conference room.

We refer to careful studies at the Technical University Dresden on calculations, evaluations and optimizations of ventilation for various variants of natural ventilation in offices [35].

5.2. Thermal comfort in office buildings

Consider the simulation of thermal comfort in office buildings under summer conditions. Energy efficient cooling of rooms and buildings becomes more and more important. Therefore, a close look to the principles of cooling methods seems to be necessary. The above-mentioned coupled simulation between the discussed CFD model and thermal building simulation delivers all information for a detailed evaluation of the thermal comfort. Different cooling methods will be discussed. The set-up in a low-energy building with identical office (or residential) rooms is shown in Figure 10. Internal loads of 540W stem from two 'persons' and technical equipment. A part of the inner loads is modelled as local convective sources in cylindrical areas at the working places of the persons marked in the figure. The simulation is performed under moderate summer conditions followed by a period of increasing outdoor temperatures, see Figure 10 (right). Boundary conditions for the temperature again are obtained using coupling of the CFD code ParallelNS with the building simulation program TRNSYS [15]. In order to evaluate the thermal comfort, snapshots from the transient simulation with transient boundary conditions are taken on the last day of the simulation period at the time of highest thermal loads.

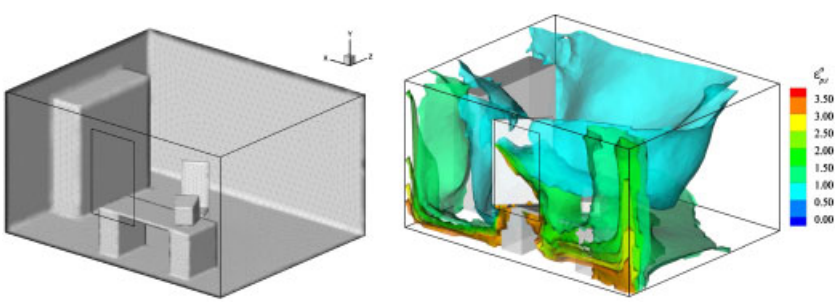

Figure 8. Natural ventilation of an office room (left) and isosurfaces of the air-exchange index (right).

DOI: 10.1002/fld

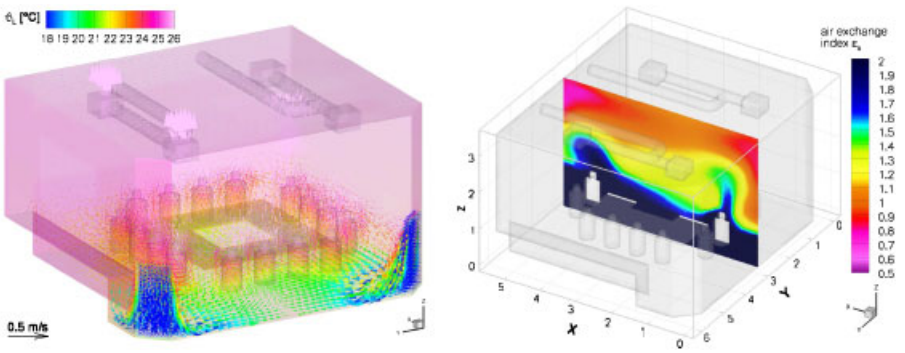

Figure 9. Displacement ventilation in a conference room with 'persons' (left) and efficiency of the ventilation (right).

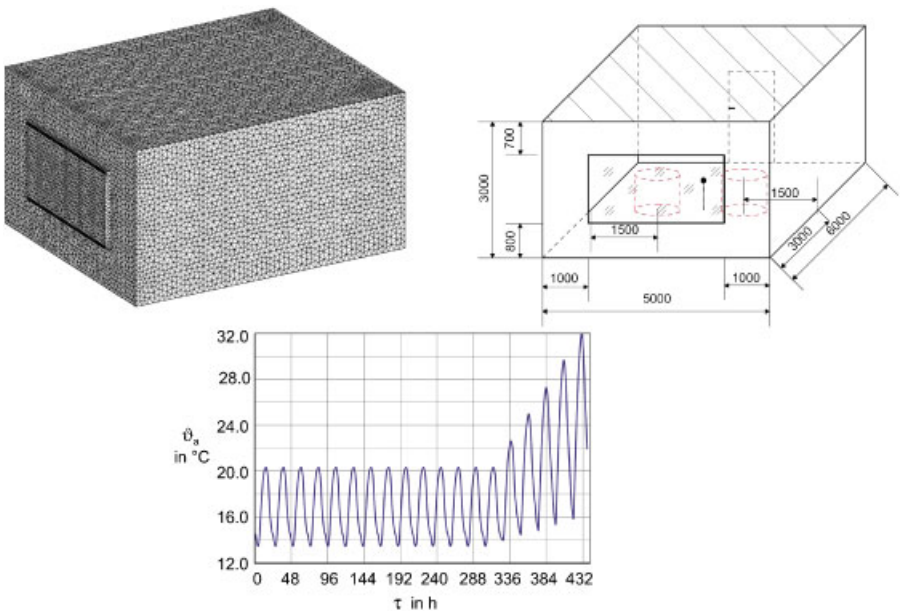

Figure 10. Low-energy building with identical offices (upper left and upper right) and outdoor temperature (bottom).

The computational domains of the investigated cases were meshed with around 300 000 tetrahedral elements. In order to verify the mesh independence, some calculations were repeated on grids with between 600 000 and 100 000 elements. The results of the mesh independence check showed in all cases, even with relatively coarse meshes, a good agreement. This is mainly due to the special wall treatment using a subgrid from the wall up to the first grid point of the tetrahedral mesh that is used in all cases. For a calculation of 1 h real time on a grid of approximately 300 000 elements, a modern personal computer needs approximately 20 h CPU time. However, this is valid only for

DOI: 10.1002/fld

the fully coupled phase, where thermal building simulation and CFD are running together. During the preparation phase, thermal building simulation is separately running, but consuming only some minutes of CPU time for several days of real time. That means for calculation of a period of 18 days (432 h, see Figure 10), consisting of 430 h preparation phase and 2 h fully coupled phase, two complete days of CPU time are necessary. As mentioned above, at the time of the highest thermal loads (this is normally in the afternoon of the last day of the simulation period), during the fully coupled phase, snapshots from the URANS simulation are taken for evaluation. In order to detect problems of thermal comfort, an additional averaging is not helpful. Snapshots from different situations at the same time and under the same conditions can be applied for comparison. The Rayleigh number for a typical calculation varies between $1.0\times10^{10}\leqslant \mathrm{Ra}\leqslant 5.0\times1.0\times10^{10}$.

At first, cooling by air with ceiling diffusors is considered. Figure 11 shows the operative temperature in the midplane and selected vertical profiles of the air temperature. The operative temperature $\vartheta_{\mathrm{op}}=\omega\vartheta_{\mathrm{L}}+(1-\omega)\vartheta_{\mathrm{R}}$ is defined as a weighted mean average of local air temperature ϑ_{L} and local radiant temperature ϑ_{R}. The radiant temperature results from radiation conditions of point to surface calculations; the weighting factor ω is 0.5 for velocities below $0.2\,\mathrm{m\,s^{-1}}$ and increases up to 0.7 for velocities higher than $0.6\,\mathrm{ms^{-1}}$, see [36, 37]. Note that the so-called occupied zone, where thermal comfort should be guaranteed, is marked with a white line in the left figure.

In Figure 12 the same situation is shown for cooling by displacement ventilation. Both situations can be compared because of the same air-exchange rate of 6/h and the same demand of the

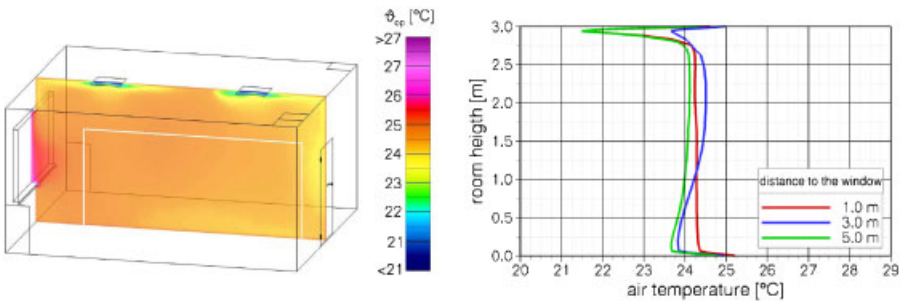

Figure 11. Ceiling diffusor: operative temperature in the midplane (left) and air temperature profiles (right).

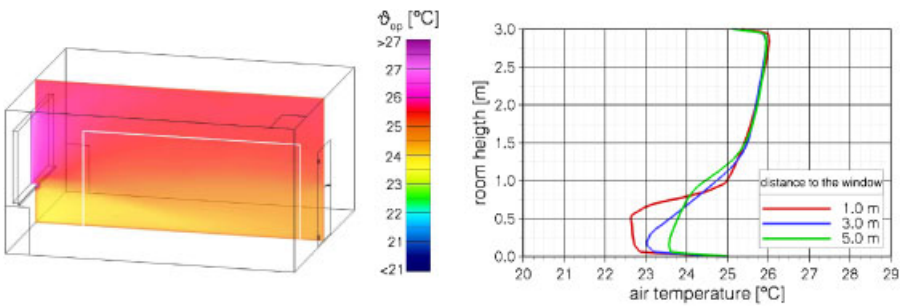

Figure 12. Displacement ventilation: operative temperature in the midplane (left) and air temperature profiles (right).

DOI: 10.1002/fld

controlling system. The operative temperature at the sensor point located in the middle of the room in a height of 0.6 m has to be 24.5°C in all cases. As mentioned above, the operative temperature comprises the effects of radiation and convection and is therefore a good measure for the thermal comfort [38]. The figures and diagrams clearly show the working principle of the cooling method. Ceiling diffusers are typical inlet devices for mixing ventilation. Therefore, almost no stratification can be recognized in the temperature profiles in Figure 11. However, in displacement ventilation a stratification is intended, as can be clearly seen from Figure 12.

Another very attractive possibility for cooling is to combine displacement ventilation with ceiling cooling. Figure 13 presents the operative temperature and air temperature profiles for that cooling method. The radiation effect of ceiling cooling permits to use higher air temperatures.

In all of the above discussed situations, only diffuse solar radiation, but not direct solar radiation, is considered. It can be constructively arranged by an overhang that prevents against direct solar radiation. However, the developed simulation program also permits to evaluate the effect of solar gains in detail. Figure 14 shows combined cooling in the case of a sun blind that reduces the direct solar radiation by 75% and diffuse solar radiation by 25%.

The operative temperature as well as the air temperature profile is influenced by the solar gains. However, the system is able to provide high thermal comfort under these conditions. The region where direct solar radiation meets the floor is marked in Figure 14.

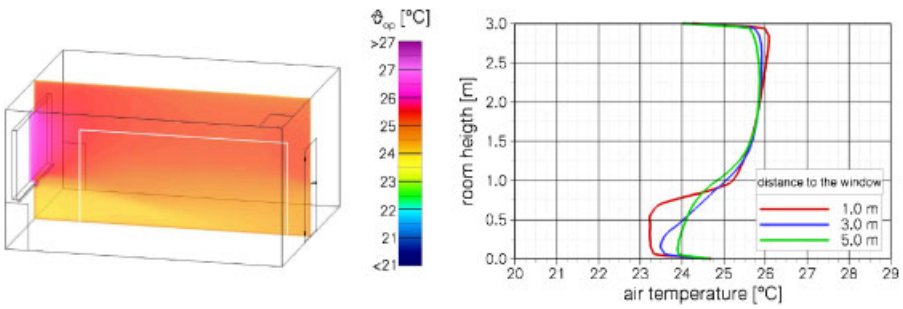

Figure 13. Combined cooling: operative temperature in the midplane (left) and air temperature profiles (right).

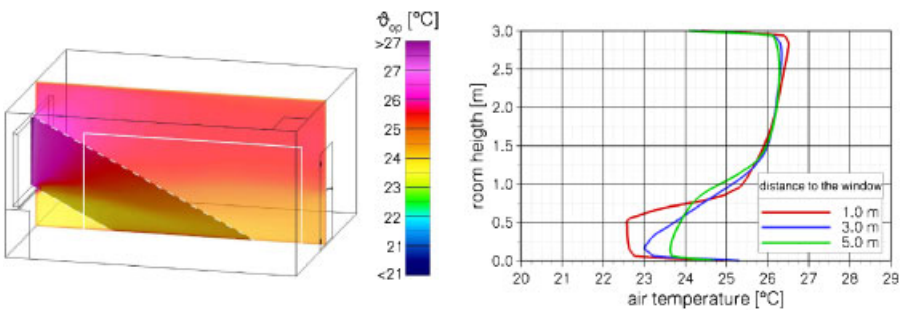

Figure 14. Combined cooling with sun blind: operative temperature in the midplane (left) and air temperature profiles (right).

DOI: 10.1002/fld

Finally, Figure 15 shows the same situation for a room with combined cooling but no solar protection. It is obvious that the compensation of high solar gains is a challenge for a cooling system. The influence on the operative temperature can be clearly seen. The corresponding inner surface temperatures are shown in Figure 16. In addition, the draught rating (DR) is calculated for a vertical plane in 0.1 m height according to ISO 7730 [36]. Draught is an unwanted local cooling of the body by air movement. It can be calculated by an empirical formula including local air temperature, local air velocity and turbulence intensity and results in a percentage of people who may be bothered by draught. For further details see [36]. It can be seen from the figures that missing solar protection in the summer (cooling) season is not only a waste of energy, it may also create problems concerning thermal comfort. The combined system is a very advanced one, pure air cooling or ceiling cooling alone will show more losses in thermal comfort and is not discussed here.

Finally, it can be seen that the developed method of stabilized FEs combined with thermal building simulation is a powerful tool for analyzing indoor air flows, especially concerning the thermal comfort. Although it is impossible to calculate every detail of the turbulent flow by the presented method and the selected turbulence model it is very helpful in engineering practice. A comprehensive investigation of thermal comfort under summer conditions from an engineering point of view can be found in [37].

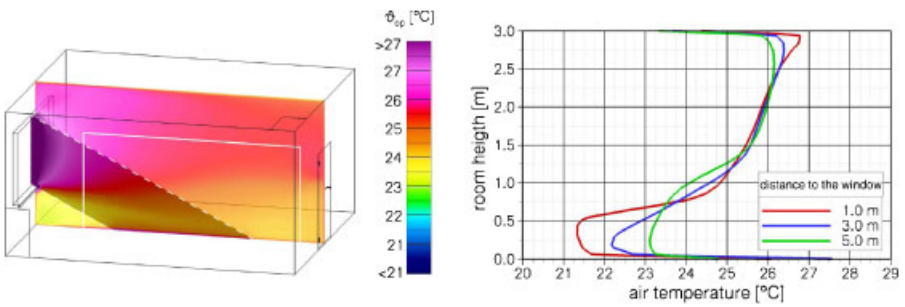

Figure 15. Combined cooling without sun blind: operative temperature in the midplane (left) and air temperature profiles (right).

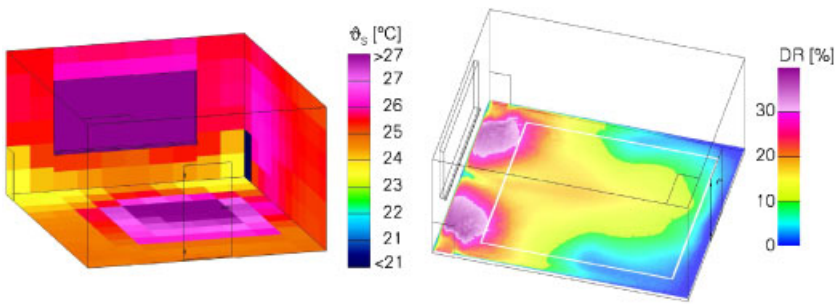

Figure 16. Combined cooling without sun blind: inner surface temperatures (left) draught rating (right).

DOI: 10.1002/fld

6. SUMMARY AND OUTLOOK

In this paper, an improved URANS turbulence model (k–ε–φ–$\overline{f}$) for turbulent indoor air flows is considered. Emphasis is put on a careful treatment of linearization regarding non-negativity of relevant quantities. We present our recent analytical results for higher-order stabilized FE methods with equal-order interpolation of velocity and pressure. In particular, we address the efficient resolution of boundary layers with anisotropic mesh refinement. Finally the approach is applied to the numerical simulation of buoyancy-driven flows. In particular, the application of criteria for the evaluation of the indoor air climate and simulation studies of thermal comfort in offices is considered.

Further research will focus on the development of efficient computational optimization tools (e.g. via domain decomposition) and on the application of LES and detached-eddy simulation for thermally driven flows.

REFERENCES

1. Hanjalic K. LES T-RANS and hybrid simulations of thermal convection at high *Ra* numbers. *International Journal of Heat and Fluid Flow* 2006; **27**:800–810.
2. Mohammadi B, Pironneau O. *Analysis of the K-Epsilon Turbulence Model*. Masson/Wiley: Paris, Chichester, 1994.
3. Tieszen S, Ooi A, Durbin P, Behnia M. Modeling of natural convection heat transfer. *Proceedings of the Summer Program 1998*, Center for Turbulence Research, Stanford University, 1998; 287–301.
4. Durbin PA, Petterson Reif BA. *Statistical Theory and Modelling for Turbulent Flows*. Wiley: Chichester, 2001.
5. Laurence DR, Uribe JC, Utyuzhnikov SV. A robust formulation of the $v2-f$ model. *Flow, Turbulence and Combustion* 2004; **73**:169–185.
6. Hanjalic K, Laurence DR, Popovac M, Uribe JC. $\overline{v^2}/k-f$ turbulence model and its application to forced and natural convection. *Proceedings of ERCOFTAC ETMM-6 Conference*. Elsevier: Amsterdam, 2005.
7. Codina R, Soto O. Finite element implementation of two-equation and algebraic stress turbulence models for steady incompressible flows. *International Journal for Numerical Methods in Fluids* 1999; **30**:309–334.
8. Lew AL, Buscaglia GC, Carrica PM. A note on the numerical treatment of the k-epsilon turbulence model. *International Journal of Computational Fluid Dynamics* 2001; **14**(3):201–209.
9. Turek S, Kuzmin D. Algebraic flux correction III. Incompressible flow problems. In *Flux-Corrected Transport*: *Principles*, *Algorithms and Applications*, Kuzmin D, Löhner R, Turek S (eds). Springer: Berlin, 2005; 251–296.
10. Lube G, Rapin G. Residual-based stabilized higher-order FEM for a generalized Oseen problem. *Mathematical Models and Methods in the Applied Sciences* 2006; **16**(7):949–966.
11. Lube G, Rapin G. Residual-based stabilized higher-order FEM for advection-dominated problems. *Computer Methods in Applied Mechanics and Engineering* 2006; **195**:4124–4138.
12. Neitzke KP. Experimentelle Untersuchung und numerische Modellierung von wandnahen thermischen Auftriebsströmungen. *Ph.D. Thesis*, TU Dresden, 1999.
13. Knopp T, Lube G, Gritzki R, Rösler M. A near-wall strategy for buoyancy-affected turbulent flows using stabilized FEM with applications to indoor air flow simulation. *Computer Methods in Applied Mechanics and Engineering* 2005; **194**:3797–3816.
14. Apel Th, Knopp T, Lube G. Stabilized finite element methods with anisotropic mesh refinement for the Oseen problem. *Applied Numerical Mathematics* 2007; DOI: 10.1016/j.apnum.2007.11.016.
15. Klein SA, Duffie JA, Beckman WA. TRNSYS—a transient simulation programm. *ASHRAE Transactions* 1976; **82**:623 ff.
16. Kays WM, Crawford ME. *Convective Heat and Mass Transfer*. McGraw-Hill: New York, 1993.
17. Martinez MJ, Gartling DK. A finite element method for low-speed compressible flows. *Computer Methods in Applied Mechanics and Engineering* 2004; **193**:1959–1979.
18. Principe J, Codina R. On the low Mach number and the Boussinesq approximations for low speed flows. *International Journal for Numerical Methods in Fluids* 2007; submitted.

19. Bernardi C, Metivet B, Pernaud-Thomas B. Couplage des equations de Navier–Stokes et de la chaleur: le modele et son approximation par elements finis. *Report 97104*, Univ. Pierre et Marie Curie, CSR, 1991.
20. Gergo L, Stoyan G. On a mathematical model of a radiating, viscous, heat conducting fluid: remarks on a paper by J. Förste. *Zeitschrift fur Angewandte Mathematik und Mechanik* 1997; **77**(5):367–375.
21. Boland J, Layton W. An analysis of the finite element method for natural convection problems. *Numerical Functional Analysis and Optimization* 1990; **11**(5/6):449–483.
22. Farhloul M, Nicaise S, Paquet L. A mixed formulation of Boussinesq equations: analysis of nonsingular solutions. *Mathematics of Computation* 2000; **69**(231):965–986.
23. Emmrich E. Analysis of time discretisations for the incompressible Navier–Stokes problem. *Ph.D. Thesis*, Cuvellier-Verlag, Göttingen, 2001 (in German).
24. Knopp T, Lube G, Gritzki R, Rösler M. Iterative substructuring methods for incompressible non-isothermal flows and its application to indoor air flow simulation. *International Journal for Numerical Methods in Fluids* 2002; **40**:1527–1538.
25. Lube G, Knopp T, Rapin G. Non-overlapping domain decomposition methods for incompressible flows. In *Mesh Partitioning Methods and Domain Decomposition Methods*, Magoules F (ed.), Saxe-Coburg, 2007; 244–274.
26. Verfürth R. Robust a posteriori error estimates for non-stationary convection–diffusion equations. *SIAM Journal on Numerical Analysis* 2005; **43**(4):1783–1802.
27. Berrone S. Adaptive discretization of stationary and incompressible Navier–Stokes equations by stabilized finite element methods. *Computer Methods in Applied Mechanics and Engineering* 2001; **190**:4435–4455.
28. Apel Th. *Anisotropic Finite Elements*: *Local Estimates and Applications*. Series Advances in Numerical Mathematics. Teubner: Stuttgart, 1999.
29. Moser TD, Kim J, Mansour NN. Direct numerical simulation of turbulent channel flow up to $Re_\tau = 590$. *Physics of Fluids* 1999; **11**:943–946.
30. Tian Y, Karayiannis T. Low turbulence natural convection in an air filled cavity, I: the thermal and fluid flow field. *International Journal of Heat and Mass Transfer* 2000; **43**:849–866.
31. Peng S-H, Davidson L. Large eddy simulation for turbulent buoyant flow in a confined cavity. *International Journal of Heat and Fluid Flow* 2001; 323–331.
32. Etheridge D, Sandberg M. *Building Ventilation—Theory and Measurement*. Wiley: New York, 1996.
33. Gritzki R, Richter W, Rösler M. How to predict the air exchange efficiency for hybrid ventilation systems. *International Journal of Ventilation* 2003; **1**(HybVent SE):33–39.
34. Perschk A, Meinhold U. Ein Modell zur hygrisch-thermischen Gebäudesimulation mit Hilfe der Kopplung von Zonen- und Feldmodell. *Bauphysik* 2007; **29**:55–62.
35. Gritzki R, Rösler M, Richter W. Vorhersage und Analyse natürlicher Lüftungsvorgänge. *Bauphysik* 2007; **29**:21–26.
36. ISO/DIS 7730. *Analytical Determination and Interpretation of Thermal Comfort using Calculation of the PMV and PPD Indices and Local Thermal Comfort*. Beuth-Verlag: Berlin, 2004.
37. Richter W. *Handbuch der thermischen Behaglichkeit—Sommerlicher Kühlbetrieb*. Schriftenreihe der Bundesanstalt für Arbeitsschutz und Arbeitsmedizin: Forschung F2071. Dresden: Dortmund, Berlin, 2007.
38. Seifert J. Zum Einfluss von Luftströmungen auf die thermischen und aerodynamischen Verhältnisse in und an Gebäuden. *Ph.D. Thesis*, TU Dresden, 2005.

DOI: 10.1002/fld